GAS TEMPERATURE AND DENSITY MEASUREMENTS BASED ON SPECTRALLY RESOLVED RAYLEIGH-BRILLOUIN SCATTERING

Richard G. Seasholtz
NASA Lewis Research Center
Cleveland, OH 44135

James A. Lock
Physics Dept., Cleveland State University
Cleveland, OH 44115

SUMMARY

The use of molecular Rayleigh scattering for measurements of gas density and temperature is evaluated. The technique used is based on the measurement of the spectrum of the scattered light, where both temperature and density are determined from the spectral shape. Planar imaging of Rayleigh scattering from air using a laser light sheet is evaluated for ambient conditions. The Cramer-Rao lower bounds for the shot-noise limited density and temperature measurement uncertainties are calculated for an ideal optical spectrum analyzer and for a planar mirror Fabry-Perot interferometer used in a static, imaging mode. With this technique, a single image of the Rayleigh scattered light can be analyzed to obtain density (or pressure) and temperature. Experimental results are presented for planar measurements taken in a heated air stream.

INTRODUCTION

Laser diagnostics based on molecular scattering are receiving increased attention for use in aerospace test facilities. These methods can provide information directly related to the parameters of the molecular state of the gas including temperature, density, and bulk velocity. Of the various molecular scattering techniques, Rayleigh scattering is the simplest and least expensive to implement. Rayleigh scattering has typically been used to obtain gas density by measuring the total Rayleigh scattered power. More information, however, is available from the spectrum of the Rayleigh scattered light.

The Rayleigh scattering spectrum is directly related to the molecular velocity distribution function, which is a function of the thermodynamic parameters (temperature, density, pressure), composition, mean velocity, and turbulence parameters. Light scattered at a single scattering angle provides information related to one component of the molecular velocities. Thus one

C-5

component of the mean velocity can be determined (from the shift of the spectral peak), and temperature and density can be determined from the spectral shape (for a low turbulence flow).

Extraction of the parameters of interest (temperature and density) from the spectrum can be accomplished by measuring the spectrum with a high resolution spectrometer, such as a Fabry-Perot or Michelson interferometer. Sharp cutoff atomic or molecular absorption filters[1,2] have also been used to measure gas temperature. Point measurements of Rayleigh scattering spectra with scanning Fabry-Perot interferometers have been used to measure temperature in a hydrogen-air flame[3,4] and velocity, density, and temperature in the exhaust of a small hydrogen-oxygen rocket[5]. Rayleigh scattering has been proposed for atmospheric temperature measurements[6,7]. In this paper we examine an imaging technique to measure density and temperature using a planar mirror Fabry-Perot interferometer. It is an extension of a 1D technique used to measure temperature and number density in a heated nitrogen jet[8] and is similar to Fabry-Perot imaging techniques for measurement of instantaneous velocity of solid surfaces[9], temperature and velocity in the upper atmosphere[10], and solar corona measurements[11].

We first analyze a hypothetical planar imaging experiment where the measurement region is illuminated with a laser light sheet, and the Rayleigh scattered light is detected with a 2D array detector. It is assumed that the medium under study is particle-free, zero-turbulence air. Cramer-Rao lower bounds are calculated for the shot-noise limited uncertainty in density and temperature measurements based on the shape of the spectrum of the Rayleigh-Brillouin scattered light.

The use of 2D spectrally resolved Rayleigh imaging is demonstrated with an experiment to map temperature and pressure in a heated air stream.

THEORY

In this section we obtain theoretical lower bounds for the uncertainty in velocity and temperature measurements for two cases where the scattered light is detected with a 2D array detector. The first case assumes that an ideal instrument is used to measure the spectrum. The second case assumes that the spectrum is measured with a Fabry-Perot interferometer operated in a static, imaging mode (this is the technique described in the Experiment section). Only errors resulting from the Poisson statistics of the detected light are considered. Thus these results represent lower bounds for measurement errors.

2D Rayleigh Scattering Diagnostic

Consider a planar imaging experiment where a laser sheet uniformly illuminates a region in the object plane corresponding to the image of an array detector having N_r rows (measured perpendicular to the beam propagation direction) and N_c columns of pixels. Let the detector pixel size be $L_x \times L_x$ (square pixels) and let the system have a magnification M (i.e., the measurement plane has dimensions $(N_c L_x \times N_r L_x)/M$). The expected number of detected photons per pixel can be written[12]

$$\langle NPP \rangle = \frac{E_l}{N_r} \frac{\epsilon n L_x \lambda_o \Omega}{hcM} \left[\frac{d\sigma}{d\Omega}\right] \tag{1}$$

where E_l is the laser energy, λ_o is the laser wavelength, $(d\sigma/d\Omega)$ is the differential Rayleigh

scattering cross section, n is the molecular number density, Ω is the solid angle of the collected light, h is Planck's constant, c is the velocity of light, and ϵ is the overall detection efficiency (including detector quantum efficiency and system losses).

As an example, consider air at NTP (T = 293K, P=1atm, $N=2.5\times10^{25}$ m^{-3}), λ_0=488nm, E_l=1J, L_x=23μm, N_r=384, M=0.5 (measurement plane = 6.6mm×4.4mm), Ω=0.05 (f/4), ϵ=0.025, and $(d\sigma/d\Omega)=8.4\times10^{-32}$ m^2/sr. For this case, equation 1 gives $\langle NPP\rangle$=770 detected photons per pixel.

Spectrum of Rayleigh Scattered Light

Quasi-elastic scattering of light by gas molecules is known as Rayleigh-Brillouin scattering[13,14]. In this scattering process, the internal energy of the scattering molecules is unchanged and the frequency of the scattered light differs only slightly from the frequency of the incident light; the frequency shifts are due to the Doppler effect on the light scattered from molecules in random thermal or collective motion. The Doppler shift for elastic scattering from a single molecule with velocity $\mathbf{v}$ is given by

$$f = \mathbf{K}\cdot\mathbf{v}/2\pi \tag{2}$$

where $\mathbf{K}=\mathbf{k}_s-\mathbf{k}_0$ with $\mathbf{k}_s$ and $\mathbf{k}_0$ being the wave vectors of the scattered and incident light, respectively. The magnitude of $\mathbf{K}$ is a function of the scattering angle θ_s and the wavelength λ

$$K = |\mathbf{K}| = (4\pi/\lambda)\sin(\theta_s/2) \tag{3}$$

The corresponding wavelength

$$\Lambda = \frac{2\pi}{K} \tag{4}$$

is the wavelength of the scattering process, or interaction wavelength.

The spectrum of the Rayleigh scattered light from a gas is a composite of the light scattered from the individual molecules in the gas. For a low density gas, the molecules can be considered as independent scatterers. And, for a single component gas with a Maxwellian velocity distribution, the normalized spectrum of the scattered light is a simple Gaussian[14]

$$S(f)\,df = \frac{2\sqrt{\pi}}{aK}\,e^{-[2\pi(f-f_0)-\mathbf{K}\cdot\mathbf{V}]^2/a^2K^2}df \tag{5}$$

where $a = (2\kappa T/m)^{1/2}$ (m = molecular mass; κ = Boltzman's constant) is the most probable molecular speed. The spectral peak is shifted from the laser frequency $f_0=c/\lambda_0$ by $\mathbf{K}\cdot\mathbf{V}/2\pi$, where $\mathbf{V}$ is the bulk velocity of the gas. Here, the spectrum is normalized so that

$$\int S(f)\,df = 1 \tag{6}$$

(Note that all integrations over frequency have limits $[-\infty,+\infty]$.)

For higher density gases, the molecular velocities become correlated and the spectrum deviates from the Gaussian form given by equation 5. At high densities, the scattering can be treated as scattering from thermally induced density fluctuations (Brillouin scattering), and the

spectrum can be calculated using relatively simple continuum (hydrodynamic) theory[15]. In this regime the spectrum is characterized by three peaks: the central peak results from scattering from non-propagating entropy fluctuations; and the side peaks result from propagating pressure fluctuations (i.e., acoustic waves). For intermediate densities the spectrum makes a transition from the Gaussian to the Brillouin spectrum. Here, the spectrum has been calculated using various kinetic theory models[16-19], with the 6-moment model of reference 18 being the best model presently available for a single species gas[20,21].

The Rayleigh-Brillouin spectrum is generally parameterized by a non-dimensional frequency shift

$$x = \frac{2\pi f'}{Ka} \tag{7}$$

and a non-dimensional quantity

$$y = \frac{p}{\mu Ka} \tag{8}$$

where p is the gas pressure and μ is the shear viscosity. The x parameter is the ratio of the frequency shift $f'=f-f_o$ to the acoustic frequency, and the y parameter is the ratio of the molecular collision frequency to the acoustic frequency (or, equivalently, the ratio of the interaction wavelength Λ to the molecular mean-free-path). For single component gases, the normalized spectrum is, in general, a function of x and y alone[22]. For low density gases, $y \to 0$; and the spectrum is the Gaussian given by equation 5, which can be written

$$S(x)\,dx = \pi^{-1/2}\, e^{-x^2} dx \tag{9}$$

where the bulk velocity is assumed be be zero.

Typical spectra calculated using the S6 model of reference 18 are shown in figure 1.* These examples are for air with a laser wavelength λ=488nm and a scattering angle θ_s=90°. The viscosity and thermal conductivity are calculated using the program described in reference 23. The transition between the Gaussian spectrum and the hydrodynamic spectrum occurs for $y \simeq 1$. Note that y = 0.75 for air at ambient temperature and pressure, which means the simple Gaussian spectrum is not appropriate.

Cramer-Rao Lower Bounds

As we are interested in applying Rayleigh-Brillouin scattering as a diagnostic for measuring the thermodynamic parameters of a gas, we find it useful to establish the theoretical lower bounds for accuracy of estimates of temperature and density based on the measurement of Rayleigh-Brillouin spectra. The lower bounds are a result of the Poisson statistics of the photon arrival rates (shot-noise limit).

The observed Rayleigh scattering spectrum can be expressed as a set of counts

$$\langle n_j \rangle = G_R\, S(f_j)\, \Delta f \tag{10}$$

which are the expected number of counts in frequency interval f_j to $f_j + \Delta f$ where G_R is the total

number of detected photons in the spectrum. The spectrum is thus a function of a set of three unknown parameters that can be expressed as the vector

$$\boldsymbol{\alpha} = [G_R, \rho, T] \tag{11}$$

where ρ is the gas density, and T is the gas temperature. Assuming that the parameters are uncorrelated, the estimate of the variance of α_i (Cramer-Rao lower bound)[24] is given by

$$V(\hat{\alpha}_i) = \frac{1}{\Gamma_{ii}} \tag{12}$$

where Γ is the Fisher information matrix given (for Poisson statistics) by[25]

$$\Gamma_{ij} = \sum_q \frac{1}{\langle n_q \rangle} \frac{\partial \langle n_q \rangle}{\partial \alpha_i} \frac{\partial \langle n_q \rangle}{\partial \alpha_j} \tag{13}$$

For this work, we want to obtain the temperature and density from the shape of the spectrum. (i.e., the total scattered power is not used). (We could just as well have selected pressure and temperature as the independent thermodynamic parameters.) Expressed as standard deviations $\sigma(\alpha_i) = [V(\alpha_i)]^{1/2}$, the lower bounds for measurement uncertainties for density and temperature are

$$\sigma(\rho) = \left[G_R \left[\frac{\partial y}{\partial \rho}\right]^{1/2} \int \frac{1}{S} \left[\frac{\partial S}{\partial y}\right] dx \right]^{-1/2} \tag{14}$$

$$\sigma(T) = \left[G_R \int \frac{1}{S} \left[\frac{\partial y}{\partial T} \frac{\partial S}{\partial y} - \frac{1}{2T}\left[S + x\frac{\partial S}{\partial y}\right]\right]^2 dx \right]^{-1/2} \tag{15}$$

For the low density limit $y \to 0$, and the Gaussian spectrum given by equation 9 can be used in equation 15 to find

$$\sigma(T)_{y=0} = (2/G_R)^{1/2}\, T \tag{16}$$

For higher densities where the spectrum is not Gaussian, the integrals in equations 14 and 15 can be numerically evaluated. Using the spectrum calculated from the 6-moment model[18] and the gas properties calculated using the FLUID program[23], the relative uncertainties for temperature and density as a function of the parameter y are shown on figure 2. Note that the temperature uncertainty decreases slowly from the low density limit with increasing y, reaching 1/2 of the low density value at y=5. The uncertainty in the density decreases with increasing y from very large values at low density. Also, note that the uncertainty in the density measurement determined from the spectral shape is at least a factor of $2^{1/2}$ larger than the uncertainty based on measurements of the total scattered light. (The relative density uncertainty based on the total scattered light is $G_R^{-1/2}$.)

Numerical Example

Consider the 2D imaging example discussed above for air at NTP, where the detected photons/pixel was $\langle NPP \rangle = 770$. For $\theta_s = 90°$ and $\lambda = 488nm$, $K = 1.821 \times 10^7 m^{-1}$, $a = 410m/sec$, and $y = 0.75$. Based on the light detected at a single pixel ($G_R = 770$), figure 2 gives the lower bound for density uncertainty $\sigma(\rho)/\rho = 27\%$, and the lower bound for temperature $\sigma(T)/T = 5\%$. Note that both uncertainties are inversely proportional to the square root of the number of pixels; e.g., for the light collected from 100 pixels, the uncertainties would decrease by a factor of 10 (and the spatial resolution would decrease by a factor of 10). Finally, it must be emphasized that these uncertainties are lower bounds based on spectral measurements with an ideal spectrum analyzer. Actual measurements using non-ideal spectrum analyzers will always give larger uncertainties.

Fabry-Perot Interferometer

The above error estimates were based on the use of an ideal instrument to measure the spectrum. In this section we perform the error estimation based on measurement of the intensity distribution of light imaged through a planar mirror Fabry-Perot interferometer (fig. 3). The expected number of detected photoelectrons $\langle NDP \rangle$ for the q_{th} pixel is

$$\langle NDP_q \rangle = \langle NPP_q \rangle \int\int S(f) I_t(f, \theta_r) df \, dA_{pixel} \tag{17}$$

where the Fabry-Perot transmission function[26]

$$I_t(\psi) = \frac{1}{1 + F \sin^2(\psi/2)} \tag{18}$$

with ψ being the phase delay of the light for one pass through the interferometer given by

$$\psi = \frac{4\pi\mu df \cos\theta_r}{c} \tag{19}$$

and $F = (2N_R/\pi)^2$, where N_R is the reflective finesse. In this equation, f is the frequency of the light, μ is the refractive index of the medium in the Fabry-Perot cavity (taken as unity here), d is the Fabry-Perot mirror spacing, and θ_r is the angle between the ray and the optic axis. For simplicity, we neglect spectral broadening due to the finite size of the aperture of the collection optics.

We now select, for this example, a particular Fabry-Perot configuration (mirror spacing $d = 15mm$; finesse $N_R = 20$) and numerically evaluate the Fisher matrix elements

$$\Gamma_{ij} = \sum_q \frac{1}{\langle NDP_q \rangle} \frac{\partial \langle NDP_q \rangle}{\partial \alpha_i} \frac{\partial \langle NDP_q \rangle}{\partial \alpha_j} \tag{20}$$

where the sum is over a 50×50 pixel subregion, giving a spatial resolution of about 0.6mm. This relatively large subregion was chosen so that it would encompass the entire width of the first (largest width) fringe. Use of subregions smaller than the fringe width result in larger

uncertainties, even for the same number of total counts in the subregion. The results of this calculation are given in Table 1 for several locations of the subregion (denoted by fringe radii). The density uncertainty is about 5% (10 times that achievable with an ideal spectrum analyzer) and the temperature uncertainty, except for the first fringe, is about 0.3% (3 times that of ideal). The larger temperature uncertainty at the first fringe is probably caused by the relatively large fringe width relative to the subregion size.

Other Error Sources

The above calculations for lower bounds of measurement uncertainties using a Fabry-Perot interferometer represent an idealized measurement process. In practice, a variety of factors will increase these calculated uncertainties. One factor is the assumption of constant finesse. The effective finesse will not be constant; vignetting reduces the effective number of reflections in the interferometer cavity, thereby decreasing the finesse at larger fringe radii. This means that the finesse must be measured, as is done in the experiment described later in this paper. Another factor is the stability of the laser frequency and Fabry-Perot interferometer alignment, which will also decrease measurement accuracy. A third factor is the assumption of a known gas composition; if the gas is made up of an unknown mixture of component gases, the spectrum cannot be uniquely related to the temperature. Also, if the flow is highly turbulent, and the measurement is obtained over a duration much greater than the turbulence time scale, the spectrum is broadened with both temperature and turbulence contributing to the spectral width. Thus, if one of these is known, the other can be determined from the spectral width, but both cannot be simultaneously determined. Finally, contaminant particles in the flow will strongly scatter. In some cases where the particle number density is low, the images can be processed to remove the obvious particles. If the particle number density is so large that the particles images overlap and cannot be removed, the spectral shape is changed from that of pure molecular scattering and density and temperature measurements cannot be obtained.

EXPERIMENT

Apparatus

An experiment (fig. 4) was conducted to demonstrate the technique discussed above to measure gas temperature and density based on the measurement of the spectrum of Rayleigh-Brillouin scattering. A commercial electric torch (9mm dia.) was used to generate the low velocity hot air stream. A co-flow arrangement, where the electric torch was located in a larger (53 mm dia.) flow of particle-free, ambient temperature air was used to eliminate particles from the measurement region. The temperature of the hot stream was measured with a thermocouple located at the center of the measurement region. As no correction was made for conduction losses, it was expected that the thermocouple temperature would be less than the actual air temperature. The beam from an argon-ion laser(2.5W, 488nm) was formed into a sheet (about 10mm high by 0.2mm thick) using a combination of cylindrical and spherical lenses. The light sheet passed through the center of the hot air stream about 17mm above the exit plane of the

torch. A 250mm focal length f/3.6 lens was used to collect and collimate the light scattered at 90°. The collimated light was passed through a planar mirror Fabry-Perot interferometer (70mm diameter aperture and 14.96mm mirror spacing) and focused onto the CCD array with a 500mm focal length lens. The CCD array had 384 rows by 576 columns of 23μm x 23μm square pixels (giving a field size in the flow of 4.4mm×6.6mm) and was cooled to about -50° C to reduce dark current. The CCD pixel data was digitized with 12 bit resolution and transferred to an 80386 PC via an IEEE-488 interface for storage and analysis.

The initial step in the measurement process was to measure the instrument function [$I_t(\psi)$, for $f=f_0$]. A diffusely scattering target was placed in the field of view and illuminated with laser light scattered from a rotating diffuse target (the rotating target was used to reduce speckle in the recorded image). The Rayleigh scattered light from the flow was then recorded. Exposure times were 0.1s for the instrument function and 10s for the Rayleigh scattering. Two images of the Rayleigh scattered light were taken, so the technique described in reference 27 could be used to reduce the effect of any residual particles.

Data Reduction

The data reduction was done in two steps. First, the instrument function image (such as figure 5a) was analyzed to determine the center of the circular fringe pattern, the finesse, and the phase corresponding to the laser frequency. Because the effective finesse and phase varied over the image plane, it was necessary to determine them as a function of location in the image (typically, the finesse varied from about 20 at the center to about 4 at the edges of the image). Seventy-seven 50×50 pixel subregions were used. The subregions were positioned evenly spaced around the fringes. A typical pattern of subregions is shown in figure 6. A 4th degree, 2D polynomial (15 parameters) was then fit to these values of phase and finesse. The coefficients for the polynomial fits were saved for the second step (analyzing the image of the Rayleigh scattered light).

In the second step, the image of the Rayleigh scattered light (fig. 5b) in each subregion was fit to a model function given by equation 10 using the 6-moment model of reference 18 with the gas properties of air. The temperature and pressure values obtained at each subregion were fit to 2D 4th degree polynomials, which were used to generate contour plots.

Results

Data were taken at ambient conditions and for two different temperatures of heated air. The centers of the 77 50×50 pixel subregions are shown in figure 6. Temperature and pressure were determined at each of the 77 subregions. (Pressure was obtained instead of density to facilitate comparison with the measured ambient static pressure.).

Ambient Condition Measurement

The measured ambient temperature and pressure were 296K and 14.35 psia. The mean temperature based on the 77 individual subregion measurements was 302K with standard

deviation 7K. The mean pressure was 14.4psia with standard deviation 0.7psia. The contour plots of temperature and pressure obtained from the 77 subregions are shown in figures 7a and 8a. As the contours are based on this set of measurements, the contours outside the region where measurements were taken should be disregarded (i.e., at the corners). Both the temperature and pressure results agree well with the actual conditions.

Heated Air Measurements

Figures 7b,c and 8b,c show contour plots for temperature and pressure taken at measured (thermocouple) air temperatures of 471K and 677K. For the higher temperature measurement, the first ring was not included in the data reduction because its width was too large relative to the subregion size, which results in decreased accuracy. The maximum temperatures shown on the contour plots are 510K and 750K. As expected, these are somewhat higher than the temperatures measured with the thermocouple. The pressure measurements, except for the inner fringe subregions, do not show the same level of agreement with the actual pressure as did the ambient temperature measurements. For the 471K flow, the mean pressure and standard deviation were 12.1psia and 1.4psia. For the 750K flow, the mean pressure and standard deviation were 9.2psia and 2.6psia. The poor results for pressure at the elevated temperatures may be explained by the smaller y parameter values corresponding to the lower densities at the higher temperatures (the y parameters were 0.72 (296K), 0.37 (510K), and 0.24 (750K)). (As discussed above, the uncertainty in density, or pressure, measurements rapidly increases as y decreases.)

The observed standard deviations in the measurements are larger than the uncertainties based only on the shot-noise limits. This indicates that for the relatively high signal levels, other sources outweigh these statistical errors. One potential error source is the drift in the Fabry-Perot mirror spacing between recording the instrument function and the Rayleigh data.

The data reduction requires rather lengthy processing, chiefly because of the numerical integration in equation 17. The time per iteration for each 50×50 pixel subregion is about 45s using a 80486/33MHz/Weitek 4167. Thus an image with 77 subregions and an average of 6 iterations requires about 6 hr to process. No attempt was made to optimize the code at this time, so it should be possible to substantially reduce the data reduction time.

CONCLUDING REMARKS

The results of this work show the feasibility of using measurements of the spectrum of molecular Rayleigh scattering as a diagnostic for measurement of both density and temperature based solely on the shape of the spectrum of the scattered light. The determination of temperature can be made at any density (provided, of course, that adequate scattered light is collected). For the same amount of collected scattered light, the temperature measurement uncertainty decreases for y on the order of or larger than unity. The density determination, however, is only feasible for higher densities, where the y parameter is on the order or larger than unity. The use of the spectral shape for density measurements offers the advantage compared to the measurement of the total scattered light in that no calibration is required. (The calibration constant, as seen in eq. 1, is a function of incident irradiance, optical collection angle and system losses.) This could be particularly significant in measurement situations where the calibration constant changes due to window contamination, laser beam wander, etc.

Although not discussed in this paper, bulk velocity is also measurable based on the shift of the peak of the Rayleigh scattered light (or on the frequency shift of Mie scattered light from particles).

The experimental results for temperature are consistent with temperature measured with a thermocouple. The pressure measurements presented agree with the actual pressure with the unheated flow, but show significant deviation with the heated flow. This is attributed to the reduced sensitivity of the technique at reduced densities. It is important to note that the results for temperature and pressure given involve no calibration or adjustable parameters. Only the gas parameters (molecular weight, viscosity), laser wavelength, and geometrical quantities (Fabry-Perot mirror spacing, scattering angle) are required.

The experimental work reported here used a CW argon-ion laser, which results in time-averaged measurements. Use of a pulsed laser and gated detection would offer several advantages. Measurements based on an image from a single laser pulse would give 2D maps of the gas parameters at an instant of time. The effect of background light, such as flame luminosity, could be greatly reduced. And particle images, if not too dense, should be easier to identify and remove from the flow field image. (A large number density of particles in the flow generally will prevent temperature and density measurements.)

Finally, care should be taken to prevent spurious laser light from reaching the receiving optics. Even though this light can be accounted for in the data reduction, it will degrade the signal-to-noise ratio and measurement accuracy. This problem is particularly severe in internal flows where it is very difficult to eliminate all spuriously scattered light. The technique described by Miles et al.[2] for blocking light at the laser frequency should be useful for high velocity flows where the frequency of the Rayleigh scattered light is shifted well away from the laser frequency.

ACKNOWLEDGEMENTS

We would like to acknowledge the efforts of Mr. Andrew Kremer, who was responsible for setting up and aligning the optical system used for the measurements. We also wish to thank Prof. G. Tenti for kindly providing us with the computer code for the 6-moment model.

REFERENCES

1. Shimizu, H.; Lee, S.A.; and She, C.Y.: High spectral resolution lidar system with atomic blocking filters for measuring atmospheric parameters, *Appl. Opt.*, vol. 22, 1983, pp. 1373-1381.

2. Miles, R.B.; Lempert, W.R.; and Forkey, J.: Instantaneous velocity fields and background suppression by filtered Rayleigh scattering, *AIAA 29th Aerospace Sciences Meeting, Reno,* 1991, AIAA paper 91-0357.

3. Cattolica, R.; Robben, F.; and Talbot, L.: (1976) The interpretation of the spectral structure of Rayleigh scattered light from combustion gases, *AIAA 14th Aerospace Sciences Meeting, Washington,* 1976, AIAA paper 76-31.

4. Pitz, R.W.; et al.: Temperature and density in a hydrogen-air flame from Rayleigh scattering, *Comb. and Flame*, vol. 27, 1976, pp. 313-320.

5. Seasholtz, R.G.; Zupanc, F.J.; and Schneider, S.J.: Spectrally resolved Rayleigh scattering diagnostic for hydrogen-oxygen rocket plume studies, *AIAA 29th Aerospace Sciences Meeting, Reno*, 1991, AIAA paper 91-0462.

6. Schwiesow, R.L.; and Lading, L. : Temperature profiling by Rayleigh-scattering lidar, *Appl. Opt.* vol. 20, 1981, pp. 1972-1979.

7. Rees, D.; et al.: The Doppler imaging system: initial observations of the auroral thermosphere, *Planet. Space Sci.*, vol. 32, ,1984, pp. 273-285.

8. Lock, J.A.; Seasholtz, R.G.; and John, W.T.: Using Rayleigh-Brillouin scattering to determine one-dimensional temperature and number density profiles of a gas flow field, *Appl. Opt.*, vol. 31, 1992.

9. Gidon, S.; and Behar G.: Instantaneous velocity field measurements: application to shock wave studies, *Appl. Opt.*, vol. 25, 1986, pp. 1429-1433.

10. Sivjee, G.G.; Hallinan, T.J.; and Swenson, G.R.: Fabry-Perot interferometer imaging system for thermospheric temperature and wind measurements, *Appl. Opt.*, vol. 19, ,1980, pp. 2206-2209.

11. Chandrasekhar, T.; Desai, J.N.; and Angreji, P.D.: Temperatures and differential line-of-sight velocities observed in the solar corona during a total solar eclipse , *Appl. Opt.*, vol. 20, 1981, pp. 2172-2173.

12. Eckbreth, A.C.: *Laser Diagnostics for Combustion, Temperature, and Species*, Abacus Press, Tunbridge Wells, Kent, 1988, p. 367.

13. Young, A.T.: Rayleigh scattering, *Physics Today*, Jan. 19, 1982, pp. 42-48.

14. Fabelinskii, I.L.: *Molecular scattering of light*, Plenum Press, New York, 1968, p. 263.

15. Clark, N.A.: Inelastic light scattering from density fluctuations in dilute gases. The kinetic-hydrodynamic transition in monoatomic gas, *Phys. Rev.*,vol. A12, 1975, pp. 232-244.

16. Sugawara, A.; and Yip: Kinetic model analysis of light scattering by molecular gases, *Phys. Fluids*, vol. 10, 1967, pp. 1911-1921.

17. Boley, C.D.; Desai, R.C.; and Tenti, G.: Kinetic models and Brillouin scattering in a molecular gas, *Can J. Phys.*, vol. 50, 1972, pp. 2158-2173.

18. Tenti, G.; Boley, C.D.; and Desai, R.C.: On the kinetic model description of Rayleigh-Brillouin scattering from molecular gases, *Can. J. Phys.*,vol. 52, 1974 ,pp. 285-290.

19. Hubert, M.; and May A.D.: The Rayleigh-Brillouin spectrum of normal and parahydrogen: A test of model solutions of the Wang-Chang Uhlenbeck equation, *Can. J. Phys.*, vol. 53, 1974, pp. 343-350.

20. Young, A.T.; and Kattawar, G.W.: Rayleigh-scattering line profiles, *Appl. Opt.*, vol. 22, 1983, pp. 3668-3670.

21. She, C.Y.; et al.: Stimulated Rayleigh-Brillouin gain spectroscopy, *Phys. Rev*, vol. A31, 1985, pp. 3733-3740.

22. Nelkin, M.; and Ghatak, A.: Simple binary collision model for Van Hove's $G_s(r,t)$, *Phys. Rev.*, vol. 135A, 1964, pp. 4-9.

23. Fessler, T.E.: *FLUID: A numerical interpolation procedure for obtaining thermodynamic and transport properties of fluids*, NASA TM X-3572, 1977.

24. Whalen, A.D.: *Detection of signals in noise*, Academic Press, New York, 1971, pp. 324-331.

25. Lading, L.; and Jensen, A.S.: Estimating the spectral width of a narrowband optical signal, *Appl. Opt.* vol. 19, 1980, pp. 2750-2756.

26. Vaughan, J.M.: *The Fabry-Perot Interferometer, History, Theory, Practice and Applications*, Adam Hilger, Bristol, 1989, Chapter 3.

27. Kay, L.; and Sadler, D.A.: A method for processing CCD images to remove cosmic rays and other randomly positioned spurious events - theory and experiment , *Measurement Science and Technology*, vol. 2, 1991, pp. 532-535.

Fringe number	Fringe radius	$\sigma(T)/T$	$\sigma(\rho)/\rho$
1	64 pixels	0.46%	3.10%
2	136	0.24	4.56
3	181	0.26	5.34
4	217	0.26	5.86
5	248	0.25	5.75
ideal		0.09	0.53

TABLE 1. Lower bounds for uncertainty in density and temperature measurements in air. $\langle NPP \rangle = 770$; 50×50 pixel area; T=300K; p=1atm.

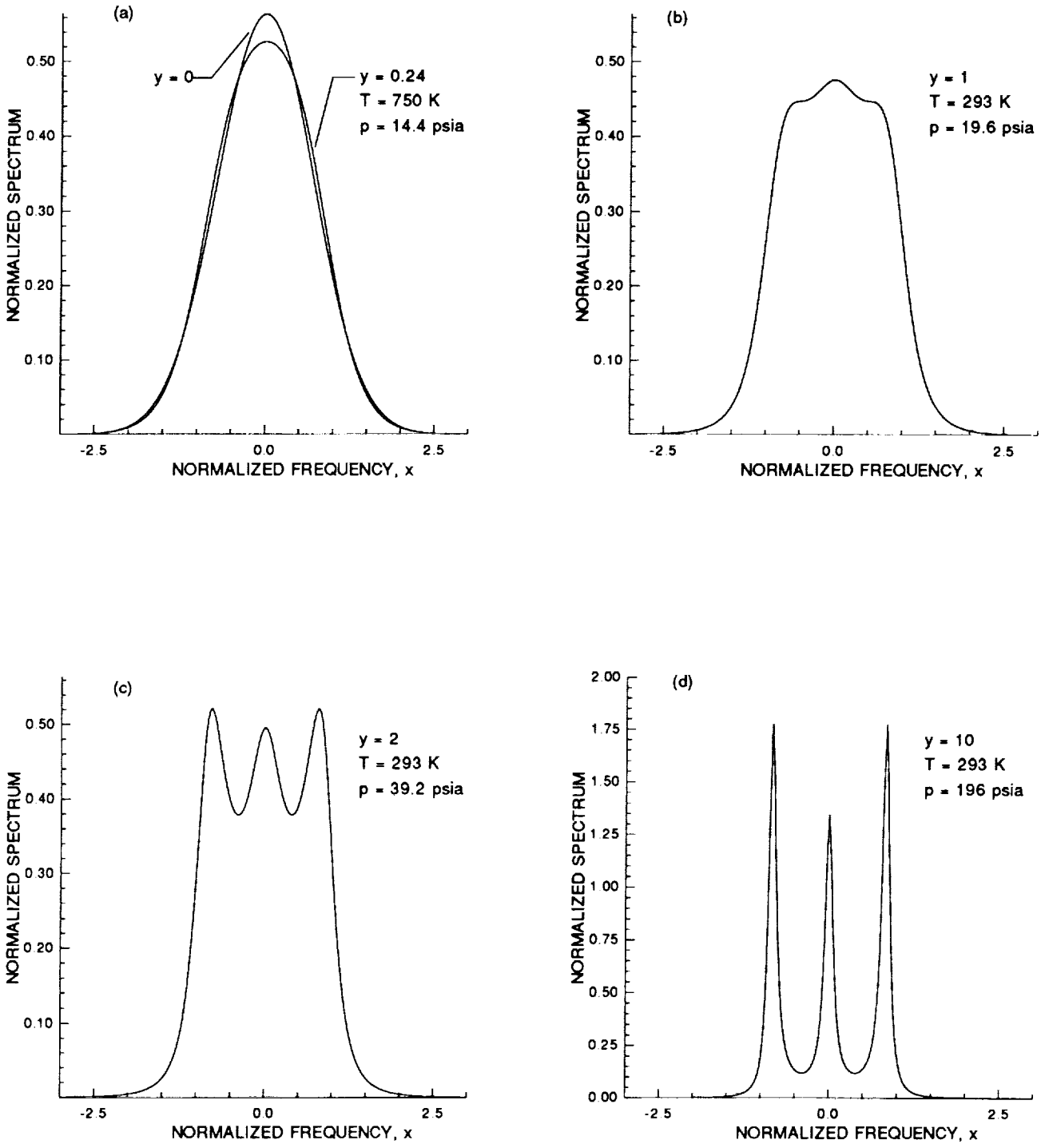

Figure 1. Calculated Rayleigh-Brillouin spectra for air K: (a) y=0,0.24, (b) y=1, (c) y=2, (d) y=10 .

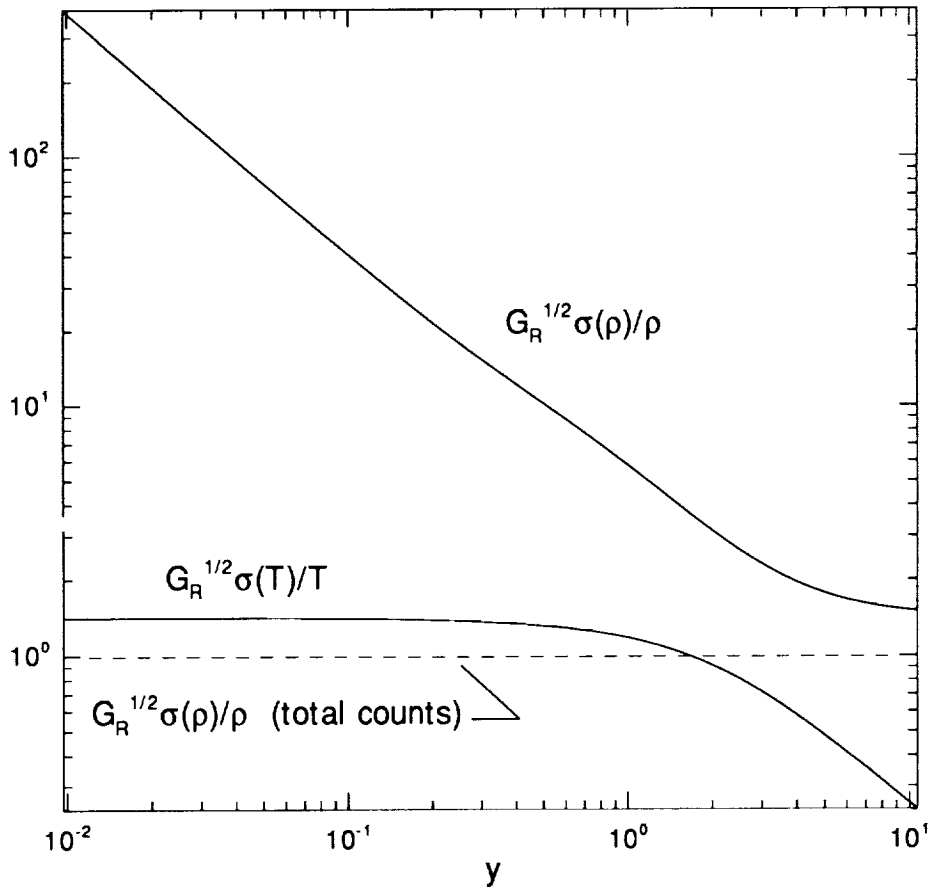

Figure 2. Cramer-Rao lower bounds for density and temperature measurement uncertainties. G_R is total number of detected photons. Dashed line is lower bound for density based on total scattered light.

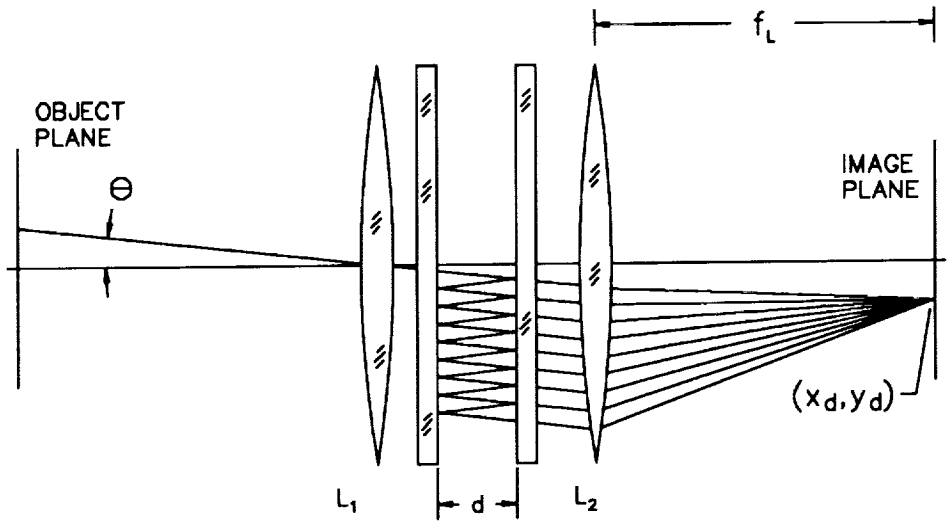

Figure 3. Fabry-Perot interferometer.

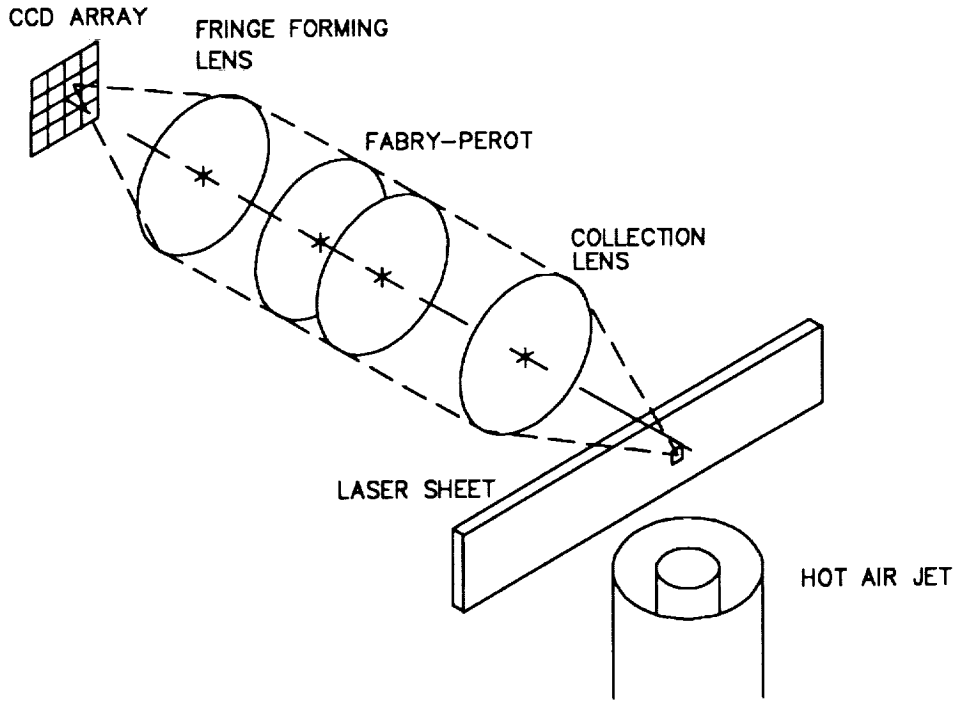

Figure 4. Experiment to map temperature and pressure in hot air stream.

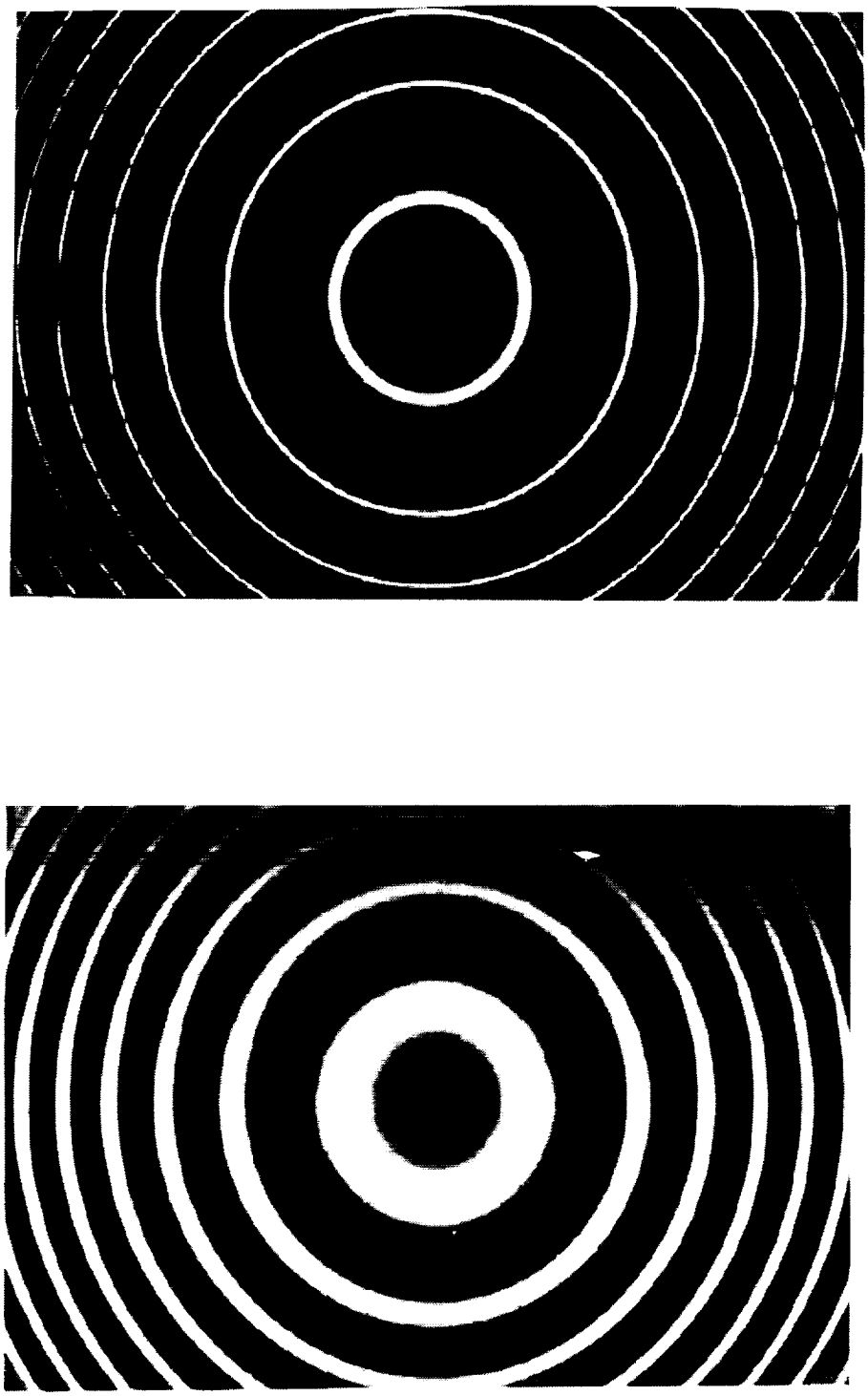

Figure 5. Fabry-Perot fringe patterns recorded with CCD camera: (a) instrument function, (b) Rayleigh scattered light.

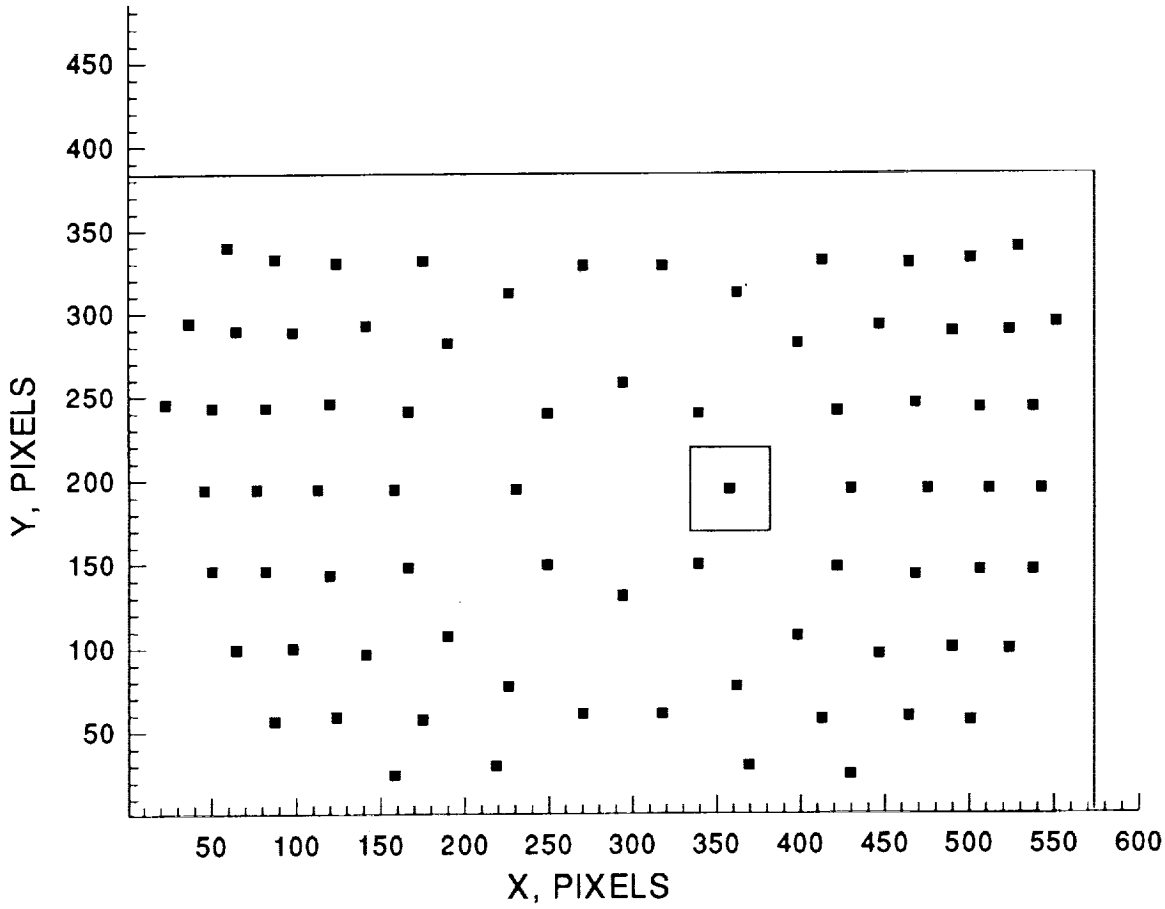

Figure 6. Pattern of subregions used for data analysis. Open box shows size of 50×50 pixel subregion.

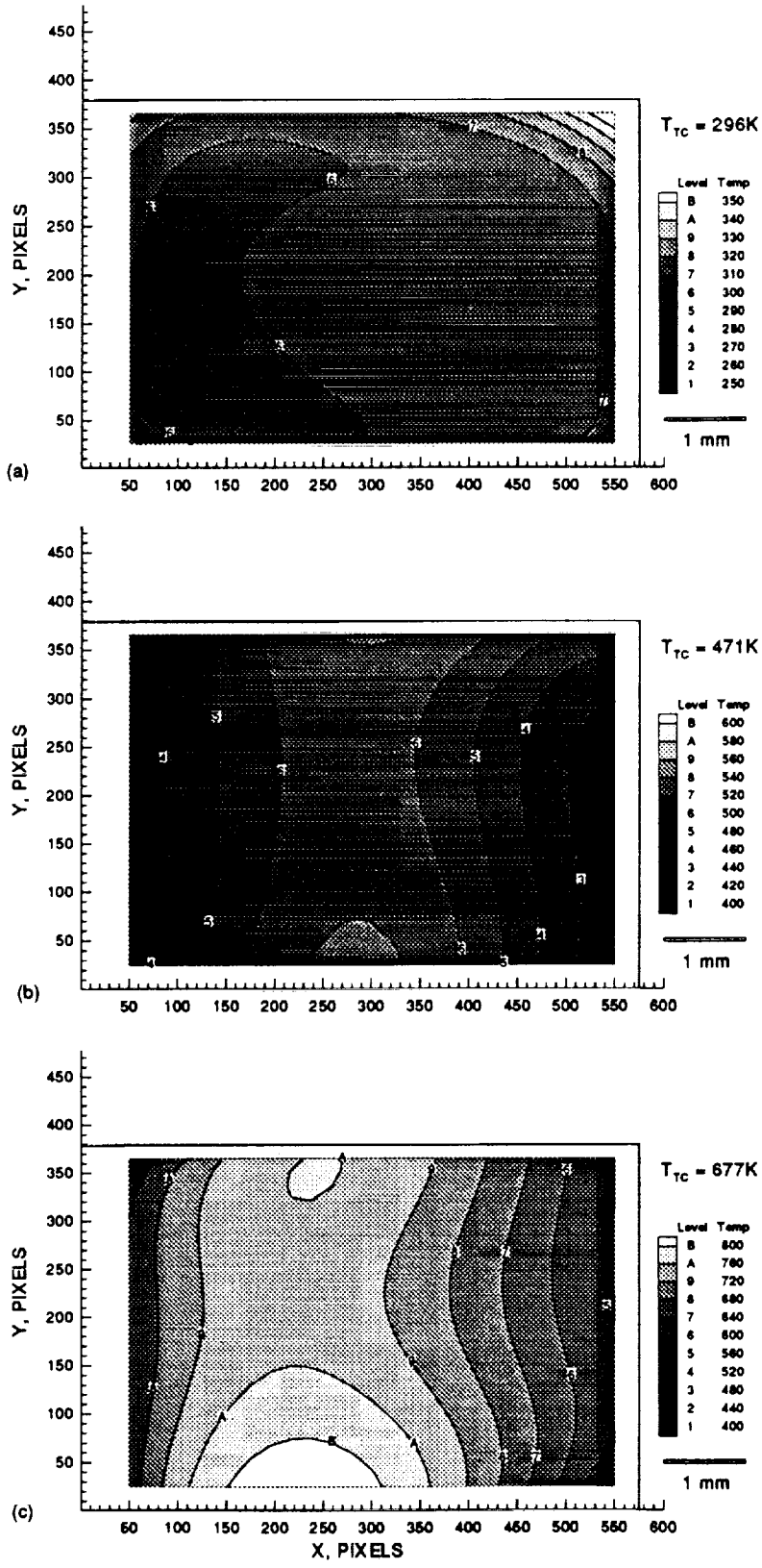

Figure 7. Contour plots of measured temperature: (a) ambient condition, T=296K, p=14.35psia (b) heated air flow, thermocouple temperature = 471K (c) heated air flow, thermocouple temperature = 677K.

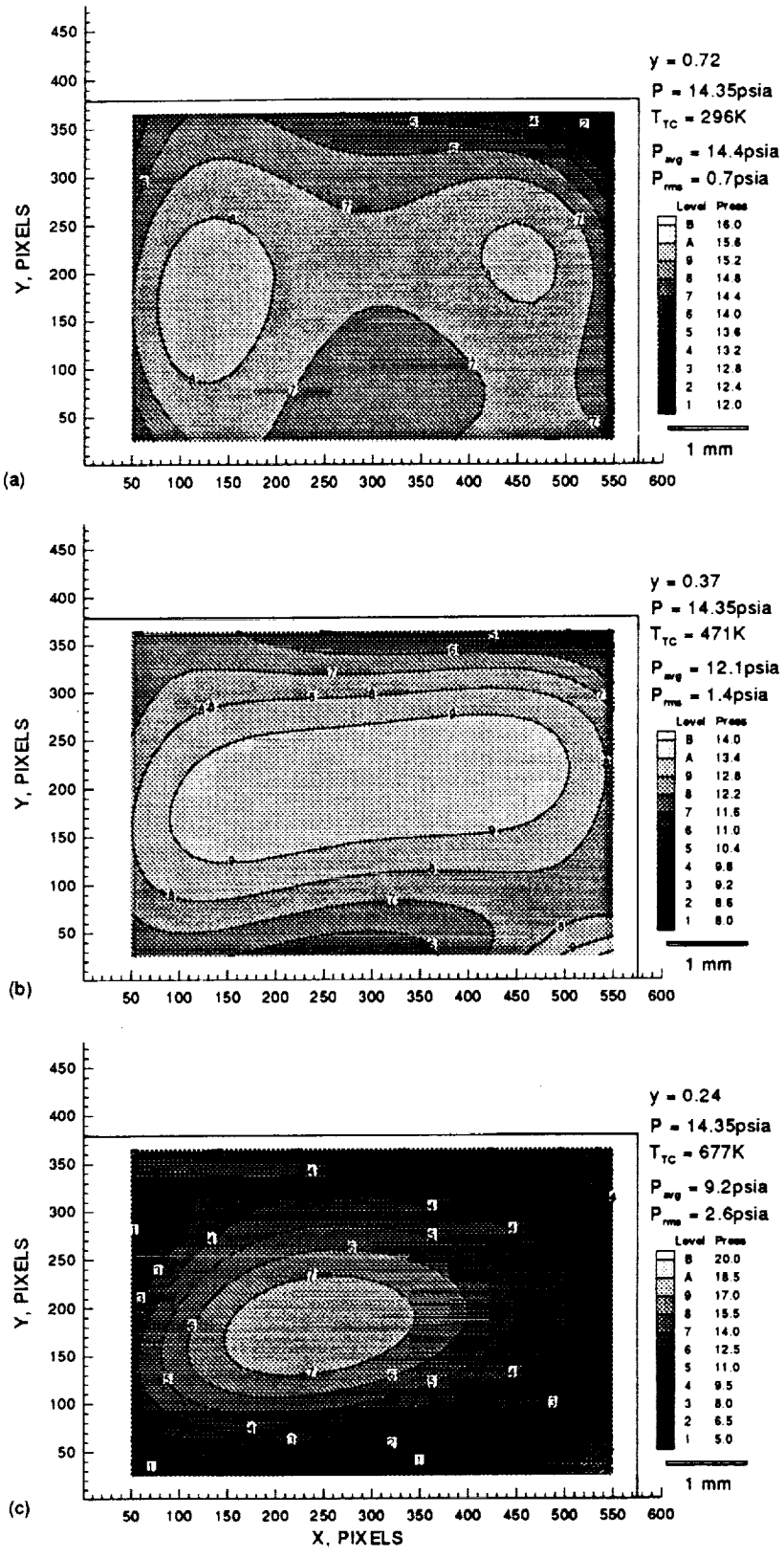

Figure 8. Contour plots of measured pressure: (a) ambient condition, T=296K, p=14.35psia (b) heated air flow, thermocouple temperature = 471K (c) heated air flow, thermocouple temperature = 677K.